Article:
Liu, F., Li, H., Gao, Z. et al. (2026) Steering charge transfer in CuInS2/BiOCl composites to enable sunlight-driven C–F bond cleavage of PFAS in water. Nature Water. ISSN: 2731-6084

https://doi.org/10.1038/s44221-026-00590-4

nature water

Article

https://doi.org/10.1038/s44221-026-00590-4

Steering charge transfer in $CuInS_2$/BiOCl composites to enable sunlight-driven C–F bond cleavage of PFAS in water

Received: 3 June 2025

Accepted: 12 January 2026

Published online: 02 March 2026

Check for updates

Fuyu Liu[1], Honglei Li[1], Zixiang Gao[1], Qiang Song[2], Patrick J. Cullen[2], Ziying Nie[3], Ye Hong[3], Yuxuan Zhang[4], Shilin Yao[5], Cheng Gu[6], Fanran Meng[7], Zhihong Zuo[8], Runzeng Liu[1] ✉, Zongwei Chen[9] ✉, Dongling Ma[10], Yongguang Yin[11], Yong Cai[12], Xiaoguang Duan[13] ✉ & Qingzhe Zhang[1] ✉

Per- and polyfluoroalkyl substances (PFAS) resist most remediation technologies because of their exceptionally inert carbon–fluorine bonds. Here we report a visible-light Z-scheme photocatalyst composed of $CuInS_2$ quantum dots anchored on BiOCl nanoplates ($CuInS_2$/BiOCl) that overcomes this barrier. Femtosecond transient absorption, steady-state spectroscopy and theoretical calculations show that an internal electric field steers photo-generated electrons (e^-) migrating to $CuInS_2$ and holes (h^+) to BiOCl, maximizing their redox potentials for simultaneous carbon–fluorine scission and carbon chain breakage, respectively. Computations revealed that benzene sulfonic acid and carbon fluoride groups on sodium *p*-perfluorous nonenoxybenzenesulfonate (OBS) are susceptible to electrophilic attack by h^+ and nucleophilic attack by e^-, respectively. Under ultraviolet irradiation, the heterojunction achieves 75.8% defluorination and 76.8% total organic carbon removal of OBS within 8 h, with universal applicability for efficient degradation of 17 representative PFAS mixtures. Continuous-flow tests driven by natural sunlight achieve >96% OBS removal in 10 h, confirming system scalability. Toxicity assays indicate negligible hazardous effects of the residual. The work reports a sunlight-powered and flow-compatible photocatalytic platform for sustained PFAS decontamination, opening a sustainable route for 'forever chemical' abatement in water.

Per- and polyfluoroalkyl substances (PFAS) represent a large group of synthetic fluorinated organic chemicals widely used as surfactants, food packaging and aqueous film-forming foam[1]. The strong C–F bond (485-540 kJ mol^{-1}) imparts innate environmental persistence and high stability to PFAS and arouses various environment-related concerns[1,2]. For example, perfluorooctanesulfonic acid and perfluorooctanoic acid, the two most notorious PFAS, have been restricted in production by >30 countries owing to their impacts on environmental and human health[3,4]. However, growing market demands for PFAS expedited the development of fluorinated alternatives. Sodium *p*-perfluorous nonenoxybenzenesulfonate (OBS) and monochlorinated-polyfluorinated-ether sulfonate (F-53B) are typical alternatives for perfluorooctanesulfonic acid[5–7]. Serious concerns regarding these fluorinated alternatives have arisen owing to their prevalence in the environment and health risks associated with long-term exposure[8,9].

One of the recognized challenges in degrading PFAS is to efficiently break C–F bonds while reducing the carbon chain length. However, most technologies reported so far rely on harsh reaction conditions such

A full list of affiliations appears at the end of the paper. ✉e-mail: rz.liu@sdu.edu.cn; zchen@zzu.edu.cn; xiaoguang.duan@adelaide.edu.au; qzz@sdu.edu.cn

as high pressure, high temperature, extra energy input and dosing of non-recyclable toxic reagents[10–12]. Therefore, exploring efficient and cost-effective strategies for the degradation and, ideally, mineralization of PFAS, particularly the new substitute OBS, from water is of great urgency. Heterogeneous photocatalysis has shown potential in PFAS degradation, considering its utilization of sustainable solar energy and operation under mild conditions[13]. Moreover, a selection of photocatalytic semiconductors can be excited by low-energy irradiation and produce reactive species, such as holes (h^+) and electrons (e^-). The photoinduced h^+ has been proven to directly attack C–C bond and lead to carbon chain shortening of PFAS[14]. The hydrated electrons (e_{aq}^-) are considered one of the most reactive nucleophilic species in breaking C–F bonds, triggering PFAS defluorination in homogeneous systems such as ultraviolet (UV)/sulfite and UV/iodide[15,16]. So far, the heterogeneous photocatalytic removal of PFAS has rarely been reported owing to the challenges in designing efficient photocatalysts system capable of making high use of both the photoinduced oxidative and reductive species. Furthermore, the very limited studies have mainly focused on the use of UVC light, which is high-energy consuming with unsatisfactory defluorination efficiency (D_f). An ideal photocatalytic system for PFAS degradation should maximize both yields and redox capacity of photo-generated h^+ and e^- to enable carbon chain shortening and C–F bond cleavage accordingly. In addition, the photocatalysts should exhibit strong light absorption and charge separation efficiency. However, achieving all these properties simultaneously within a single-component system remains inherently challenging owing to their often-conflicting material requirements.

Building upon the insights into natural photosynthesis, we developed a Z-scheme heterojunction to preserve the high redox capabilities of charge carriers and realize broadband response[17,18]. BiOCl with a low valence band (VB) position (2.34 eV versus normal hydrogen electrode)[19], and $CuInS_2$ with a high conduction band (CB) position (approximately −3.3 to −3.5 eV versus vacuum)[20], have also been explored to construct the Z-scheme heterojunction. For PFAS degradation, BiOCl can act as the oxidative component to promote carbon chain shortening[21], while $CuInS_2$ functions as a reductive component for C–F cleavage. Furthermore, the quantum dots (QDs) of $CuInS_2$ offer extra benefits of highly tunable bandgap and band-edge positions owing to the quantum confinement effect[22] and high specific surface areas, providing more active sites for PFAS adsorption and degradation. Taking all into consideration, constructing a Z-scheme heterojunction between BiOCl and $CuInS_2$ QDs presents a promising strategy for efficient PFAS degradation. In this configuration, photo-excited e^- and h^+ will be retained in the CB of $CuInS_2$ and VB of BiOCl, respectively, maximizing the redox capacity of the composite system. Furthermore, the spatial separation of charge carriers minimizes their recombination, leading to enhanced photocatalytic performance.

Intrigued by this conceptual framework, we designed and synthesized Z-scheme photocatalysts based on zero-dimensional $CuInS_2$ QDs loaded on two-dimensional BiOCl nanoplates ($CuInS_2$/BiOCl) (Fig. 1a). Both stable-state and transient measurements and density functional theory (DFT) calculations revealed that the direct attack by photo-generated e^- and h^+ contributed to the C–F bond cleavage and carbon chain shortening, respectively. A continuous-flow reactor was developed to treat PFAS-contaminated water under natural sunlight. In addition, the photocatalytic degradation of the PFAS mixture was conducted. This comprehensive investigation represents the first demonstration of Z-scheme utilization in PFAS degradation under visible light and natural sunlight and the associated mechanisms of synergistic C–F bond cleavage and photooxidation.

Results and discussion

Synthesis and characterization of $CuInS_2$/BiOCl nanocomposites

$CuInS_2$ QDs and BiOCl nanoplates were synthesized by using colloidal and hydrothermal methods modified from previous works[21,23], respectively. As illustrated in Fig. 1a, $CuInS_2$ QDs were capped with hydrophobic oleylamine (OLA) ligands. OLA–capped $CuInS_2$ QDs underwent ligand exchange to obtain hydrophilic S^{2-}-capped $CuInS_2$ QDs, which were then anchored onto BiOCl nanoplates via the strong coordination effect between S and Bi. A series of x-$CuInS_2$/BiOCl composites with x wt% of $CuInS_2$ loading content were prepared. The precise $CuInS_2$ QDs loading was quantified using an inductively coupled plasma optical emission spectrometer (see Supplementary Table 3 for details).

X-ray diffraction (XRD) patterns (Fig. 1b) revealed that BiOCl and $CuInS_2$ were well indexed to tetragonal BiOCl (JCPDS no. 85-0861)[24] and wurtzite $CuInS_2$ (JCPDS no. 77-9459)[25], respectively. Transmission electron microscopy (TEM) was used to observe the morphologies of the as-synthesized BiOCl, $CuInS_2$ QDs and $CuInS_2$/BiOCl materials. BiOCl showed a well-defined square nanoplate with a length of ~200 nm (Supplementary Fig. 1) and a thickness of ~21 ± 2 nm (Fig. 1c), which was determined by atomic force microscopy. Monodispersed $CuInS_2$ QDs with diameters of 10.3 ± 2.1 nm (Fig. 1d) were successfully loaded onto the edges of BiOCl nanoplates (Fig. 1e). High-resolution TEM (HRTEM) images clearly show the lattice fringes of the $CuInS_2$/BiOCl nanocomposites (Fig. 1f,g). The $CuInS_2$ QDs showed distinct lattice spacings of 0.31 and 0.34 nm, corresponding to the (112) facet of chalcopyrite $CuInS_2$ and the (100) facet of wurtzite $CuInS_2$, respectively[23]. A distinctive lattice fringe spacing of 0.28 nm with an angle of 90° was observed, which perfectly agrees with the (110) facet of tetragonal BiOCl[21]. To further elucidate the interfacial coupling of the two components, atomic-resolution HRTEM imaging and detailed lattice analysis were conducted. As shown in Supplementary Fig. 2, the lattice spacings of two subunits at spots (1) and (3) were measured as 0.28 and 0.34 nm, corresponding to the BiOCl (110) and wurtzite $CuInS_2$ (100) facets, respectively[23,26]. The lattice-overlap and spacing analyses at the interface region (Supplementary Fig. 2) clearly demonstrated intimate contact between BiOCl and $CuInS_2$, with their crystalline structures remaining unchanged after the coupling process. Contrast variation in the atomic-resolution image (Fig. 1g) clearly visualized the overlap and coherent contact at the interface, providing strong interfacial coupling between the two components. The corresponding fast Fourier-transform patterns further confirmed the tetragonal crystalline phase of BiOCl and the chalcopyrite and wurtzite crystalline phases of $CuInS_2$ in the interior (Supplementary Fig. 3). At the interface of the two subunits, four distinct sets of diffraction spots can be identified (Fig. 1g, insert). The energy-dispersive X-ray spectroscopy elemental mappings further confirmed the successful loading of $CuInS_2$ QDs onto BiOCl nanoplates with the formation of intimate interfaces (Fig. 1h).

To explore the local configurations of Bi atoms and atomic-level interactions between $CuInS_2$ QDs and BiOCl in the $CuInS_2$/BiOCl heterojunction, X-ray absorption near-edge spectroscopy (XANES) and extended X-ray absorption fine structure (EXAFS) analysis were conducted. As shown in Fig. 1i, a peak shift towards lower binding energy was observed on the Bi L_3 edge of $CuInS_2$/BiOCl, reflecting that BiOCl attracts electrons after coupling with $CuInS_2$ QDs[17]. The peaks at ~2.2 Å in Bi L_3-edge EXAFS of BiOCl could be assigned to the Bi–O configuration (Fig. 1j, Supplementary Fig. 4 and Supplementary Table 4). Notably, a peak around ~2.6 Å was observed and identified as Bi–S coordination in $CuInS_2$/BiOCl, which demonstrates intimate interfacial interactions between $CuInS_2$ QDs and BiOCl via Bi–S bonding (Fig. 1j, Supplementary Fig. 4 and Supplementary Table 4). The formation of $CuInS_2$/BiOCl heterojunction was also supported by the X-ray photoelectron spectrometry (XPS) measurements (Supplementary Figs. 5 and 7). The formation of $CuInS_2$ QDs structure was confirmed by XPS analysis (Supplementary Fig. 6). Notably, Bi 4*f*, O 1*s* and Cl 2*p* XPS spectra of $CuInS_2$/BiOCl showed a peak shift towards lower binding energy compared with that of pristine BiOCl (Supplementary Fig. 7). The above XANES and XPS analysis revealed the strong interfacial electronic coupling and the formation of intimate heterojunctions between $CuInS_2$

https://doi.org/10.1038/s44221-026-00590-4

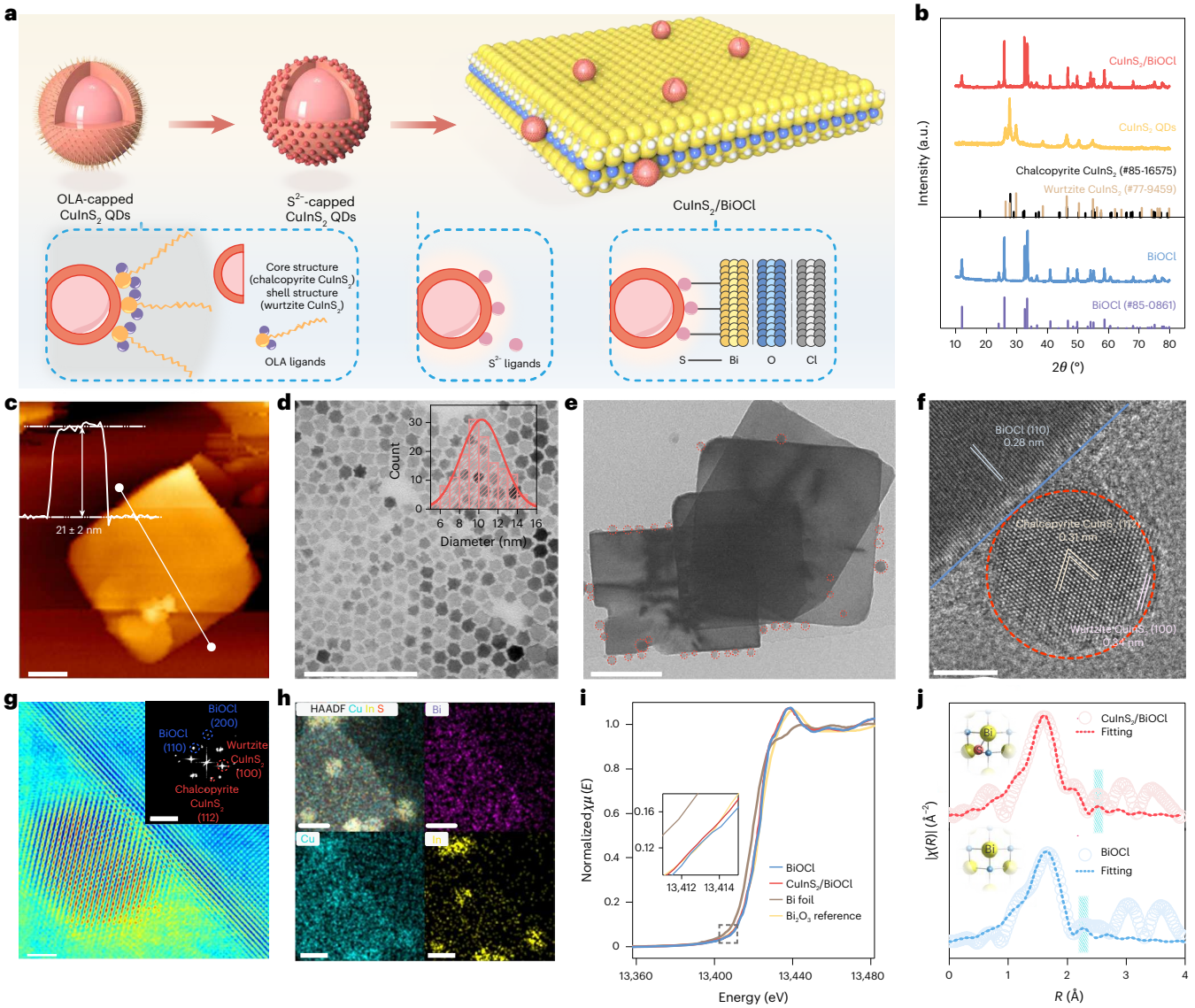

Fig. 1 | Synthesis and characterization of $CuInS_2$/BiOCl. a, A schematic illustration of synthesis procedures of $CuInS_2$/BiOCl samples. **b**, XRD patterns of BiOCl, $CuInS_2$ QDs and $CuInS_2$/BiOCl samples. **c**, Atomic force microscopy image of BiOCl. **d**,**e**, TEM images of $CuInS_2$ QDs (**d**) and $CuInS_2$/BiOCl (**e**), respectively. **f**, HRTEM images of $CuInS_2$/BiOCl. **g**, False-colour atomic-resolution HRTEM image of $CuInS_2$/BiOCl and corresponding deviated fast Fourier transform from the interface. **h**, High-angle annular dark-field (HAADF) image and elemental mappings of $CuInS_2$/BiOCl. **i**, Bi L_3-edge XANES plots. $\chi\mu(E)$ represents the X-ray absorption intensity at a given photon energy (E). **j**, Curve-fitting analysis of EXAFS spectra. Scale bars, 100 nm for **c**–**e**, 2 nm for **f** and **g**, 20 nm for **h**, 1/5 nm for insert.

and BiOCl, which could greatly facilitate the heterointerface charge transfer and promote photocatalysis.

Photocatalytic degradation and detoxication of OBS in water

Photocatalytic degradation of OBS was performed in the presence of the as-prepared photocatalysts under visible light ($\lambda > 420$ nm) irradiation (Fig. 2a,c) after adsorption–desorption equilibrium (see Supplementary Fig. 8 for details). The data fit well with the pseudo-first-order reaction model, and the rate constants (k) were calculated on the basis of this model (Supplementary Fig. 9). As shown in Fig. 2a, no OBS degradation was observed in the absence of catalysts. The pristine BiOCl and $CuInS_2$ also exhibited limited efficiency in OBS degradation, achieving only 22.6% and 16.9% removal in 90 min, respectively. This suboptimal performance is attributed to rapid charge carrier recombination and insufficient redox potential of the photo-generated species. By contrast, the $CuInS_2$/BiOCl composites exhibited greatly enhanced photocatalytic performance. The OBS removal efficiencies for 5-$CuInS_2$/BiOCl, 10-$CuInS_2$/BiOCl and 20-$CuInS_2$/BiOCl reached 55.7%, 95.4% and 39.0% (Fig. 2a). Among them, the 10-$CuInS_2$/BiOCl composite exhibited the highest rate constant ($k = 0.036$ min^{-1}), which is approximately 13 and 18 times greater than those of BiOCl (0.0027 min^{-1}) or $CuInS_2$ (0.0020 min^{-1}) alone, respectively (Supplementary Fig. 9). The striking performance enhancement in removing OBS by 10-$CuInS_2$/BiOCl should be attributed to the formed heterojunction that promoted the interfacial charge transfer and subsequent surface redox reactions. However, the excessive $CuInS_2$ QDs loading over 10 wt% could prohibit charge transfer of $CuInS_2$/BiOCl (Supplementary Fig. 10), resulting in the decreased k value for 20-$CuInS_2$/BiOCl (Supplementary Fig. 9).

The optimal sample, 10-$CuInS_2$/BiOCl, was used to further study the defluorination and mineralization of OBS under simulated sunlight irradiation (Fig. 2b). The D_F of 10-$CuInS_2$/BiOCl reached ~60% after 24-h irradiation, which was nearly three times that of BiOCl. The introduction of $CuInS_2$ QDs with a higher CB position rendered the

https://doi.org/10.1038/s44221-026-00590-4

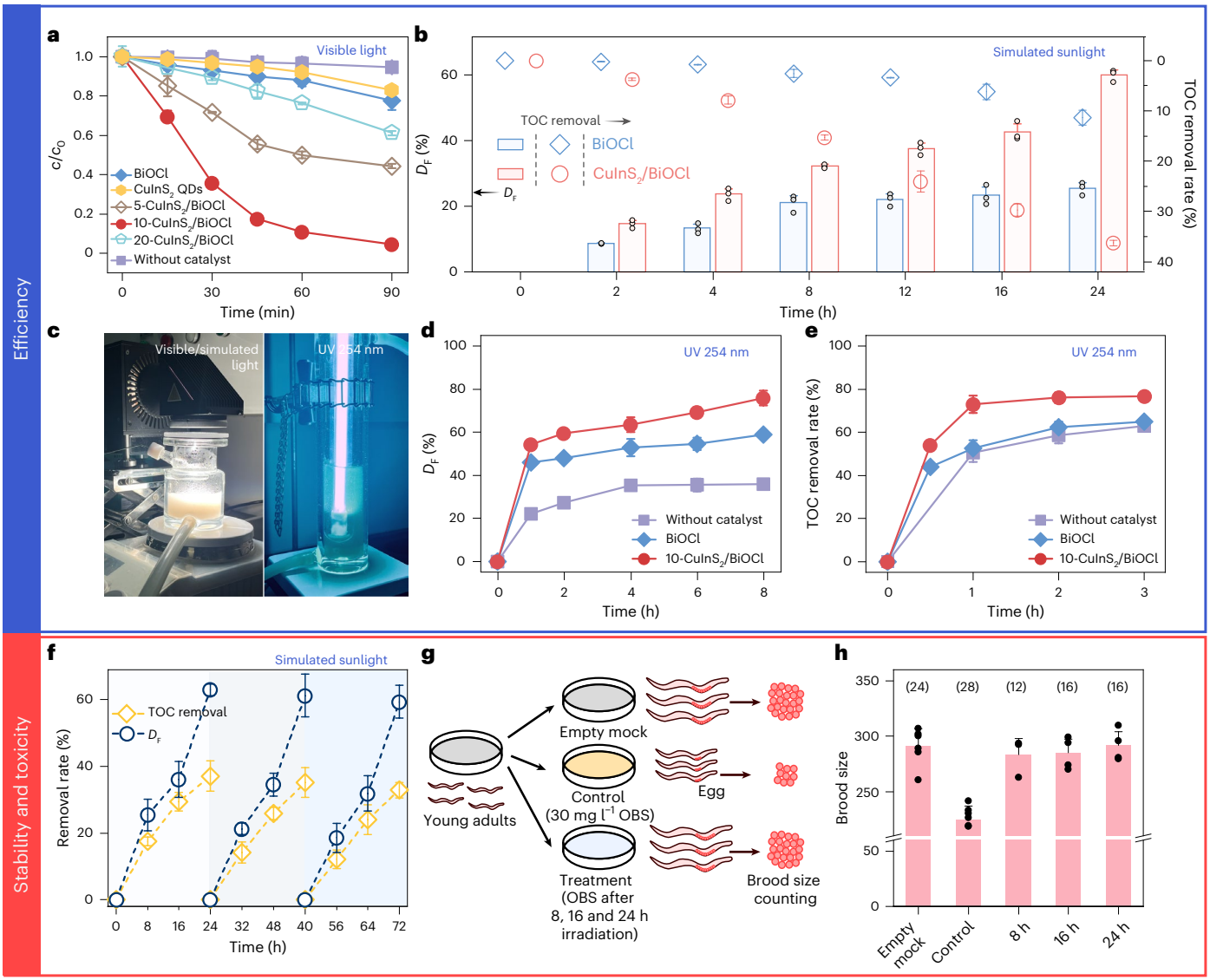

Fig. 2 | Photocatalytic degradation of OBS. a, OBS degradation under visible-light irradiation ($\lambda > 420$ nm) by BiOCl, $CuInS_2$ QDs and $CuInS_2$/BiOCl. **b**, Defluorination efficiency (D_F) and TOC removal rate by BiOCl and 10-$CuInS_2$/BiOCl under simulated sunlight. **c**, Photographic images of experimental devices for different light exposure. **d**,**e**, D_F (**d**) and TOC removal efficiency (**e**) of OBS by BiOCl and 10-$CuInS_2$/BiOCl under UV irradiation. **f**, Three cycles of OBS degradation by 10-$CuInS_2$/BiOCl under simulated sunlight. **g**, The experimental scheme of toxicological analysis. All photocatalytic experiments in **a**, **b** and **d**–**f** were performed with $n = 3$ independent reaction systems. **h**, Brood size of wild-type strains cultivated with OBS or treated OBS solution. The sample size (n, worms) is given in parentheses. The error bars represent the standard deviation (mean values ± s.d.).

photo-generated e^- of the $CuInS_2$/BiOCl system with strong reduction potential, facilitating the C–F bond cleavage and thus contributing to the boosted defluorination[15,27]. $CuInS_2$/BiOCl and BiOCl achieved total organic carbon (TOC) removal efficiencies of 36.3% and 11.4%, respectively. The molecular structure of OBS can be broadly divided into two segments: the fluorinated moiety and the benzene ring structure. Generally, the release of F^- is usually accompanied by the cleavage of C–C bonds, known as a decarboxylation–hydroxylation–elimination–hydrolysis (DHEH) pathway[28,29]. However, the branched architecture of OBS molecule exposes more peripheral C–F bonds than linear PFAS, potentially facilitating defluorination.

Intermediates and degradation products were analysed by high-performance liquid chromatography (HPLC) with high-resolution mass spectrometry (see Supplementary Fig. 11 and Table 5 for details). Various short-chain fluorinated compounds (for example, P-110, P-97 and P-127) were detected, with their concentrations increasing over the course of treatment (Supplementary Fig. 12). By contrast, the concentrations of bulkier fluorinated products (for example, P-564, P-534 and P-379) exhibited a rise-and-fall trend. The above observations indicate that the TOC removal is attributed to spontaneous defluorination and C–C breakage within the fluorinated moiety. UV light has been generally employed in current wastewater treatment plants to kill bacteria existing in the tailwater. To make full utilization of high-energy UV light, the photocatalytic degradation of OBS was performed under UV exposure (Fig. 2c–e). Differing from visible and simulated sunlight, high-energy UV photons can decompose OBS molecules in the absence of catalysts, considered as a consequence of direct photolysis of singlet oxygen[5]. The presence of BiOCl showed limited enhancement in defluorination rate (58.9%) and TOC removal efficiency (65.1%) compared with the sole UV system. The unsatisfactory performance may be attributed to the fast recombination of photo-generated charge carriers in excited BiOCl, which limits the availability of reactive species. However, $CuInS_2$/BiOCl exhibited enhanced D_F and TOC removal of OBS, reaching 75.8% and 76.8%, respectively,

which are among the reported highest values for the synchronous defluorination and degradation of OBS (Supplementary Table 6). The defluorination and TOC removal of OBS experienced a two-stage kinetic profile owing to the increased persistence of byproducts with shortened carbon chains[5,30]. Although a slight decline in activity was observed after three cycles (Fig. 2f), the nearly unchanged XRD patterns (Supplementary Fig. 13) and morphological features (Supplementary Fig. 14) after 24-h irradiation demonstrated the excellent structural stability of the $CuInS_2$/BiOCl composites. Inductively coupled plasma mass spectrometry analysis further revealed only minimal Cu (0.326%) and In (0.059%) leaching after 3 days of simulated sunlight irradiation (Supplementary Fig. 15), with concentrations well below the World Health Organization drinking water limits. These results confirm the excellent long-term stability of the $CuInS_2$/BiOCl composites during photocatalytic treatment operation.

Toxicological analysis of the degradation products was deemed necessary to check whether the toxicity of OBS was reduced after treatment. As shown in Fig. 2g, we first examined the effects of the initial concentration of OBS (30 mg l^{-1}) on the brood size of *Caenorhabditis elegans* (*C. elegans*), one of the simplest model organisms[31]. Compared with the wild type, the brood size of *C. elegans* cultivated with OBS showed a substantial reduction by 23%, indicating the reproductive toxicity of the untreated solution (Fig. 2h). By contrast, the *C. elegans* cultivated with treated OBS solution showed the similar brood size with the wild type, suggesting the negligible toxicity of the degradation products in the $CuInS_2$/BiOCl treated system. To further corroborate these findings, zebrafish embryo toxicity tests were conducted (Supplementary Fig. 16). For the blank sample without adding OBS, embryos hatched within 72 h of incubation. When exposed to OBS solution, no embryos hatched, even after 96 h. After photocatalytic treatment, the solution was used for zebrafish embryo incubation. The embryos successfully hatched within 72 h, which was the same as in the blank case, suggesting negligible toxicity of the treated OBS solution. Moreover, quantitative structure-activity relationships-based toxicity predictions indicated a notable reduction in toxicity for most degradation intermediates and products identified by HPLC coupled with high-resolution mass spectrometry (Supplementary Fig. 17). Therefore, these multilevel bioassays and computational analyses consistently demonstrated that the degradation products after photocatalytic treatment by $CuInS_2$/BiOCl exhibited notably reduced and negligible toxicity.

Mechanistic understanding of the enhanced PFAS degradation performance

The photocatalytic activity is highly dependent on the redox capability and separation efficiency of photoexcited charge carriers, which are determined by the electronic states and band structures of the photocatalysts. We thus employed UV–visible diffuse reflectance spectra and VB-XPS to measure the band structure and alignments. Based on the Kubelka–Munk analysis and VB-XPS results, the bandgaps, VB and CB edges of BiOCl and $CuInS_2$ QDs were calculated (Supplementary Figs. 18 and 19). The staggered band alignments comply with the characteristics of direct Z-scheme or type-II heterojunctions.

DFT calculations determined the work functions (W_F) of BiOCl and $CuInS_2$ as 6.99 and 4.97 eV, respectively (Supplementary Figs. 20–23). As illustrated in Fig. 3a, spontaneous electron transfer occurs from $CuInS_2$ to BiOCl until Fermi level equilibrium is reached, resulting in the formation of an interfacial electric field (IEF) across the heterostructure interface[32]. This directional charge redistribution is consistent with the XPS (Supplementary Fig. 7) and XANES (Fig. 1i) results. The presence of IEF drives the oriented migration of photo-generated electrons from CB of BiOCl to VB of $CuInS_2$ under light excitation, following the Z-scheme charge transfer pathway (Supplementaty Fig. 24). Figure 3b shows the simulated charge distribution profile and the corresponding three-dimensional charge density difference plot of $CuInS_2$ (100)/BiOCl (110) surface. The yellow and blue–green regions were observed on $CuInS_2$ (100) and BiOCl (110) facets, corresponding to the electron depletion and accumulation layers, respectively. The Bader charge analysis further confirmed the electron-donating tendency of $CuInS_2$ (Supplementary Table 7), indicating the charge transfer from $CuInS_2$ to BiOCl upon heterostructure formation. Kelvin probe force microscopy measurements were conducted to further corroborate the IEF formation. In general, an increase in the contact potential difference (V_{CPD}) corresponds to enhanced surface h^+ accumulation, whereas a decrease reflects e^- enrichment[33–35]. For the $CuInS_2$/BiOCl composites, the V_{CPD} value on the $CuInS_2$ QDs surface was higher than that on BiOCl under dark conditions (Supplementary Fig. 25), indicating that BiOCl is relatively electron-rich while $CuInS_2$ QDs are hole-rich after contact. This difference clearly demonstrates charge transfer from $CuInS_2$ QDs to BiOCl and the establishment of an IEF directed from $CuInS_2$ towards BiOCl upon contact in the dark. To further elucidate the formation of the Z-scheme heterostructure, in situ XPS was conducted to analyse the electron transfer process under light illumination. The binding energy of Bi 4*f* shifted positively by ~0.2 eV after 15 min irradiation and changed back to the 'dark state' as soon as light-off, indicating electron depletion in BiOCl (Fig. 3c). Meanwhile, the Cu 2*p* binding energy exhibited a negative shift opposite to that of Bi 4*f*, indicating electron accumulation in $CuInS_2$ (Fig. 3d). This result further convinced the photoinduced electron transfer pathway from $CuInS_2$ to BiOCl. These observations are fully consistent with the Z-scheme charge transfer pathway, in which e^- migrate to $CuInS_2$ QDs and h^+ to BiOCl under the driving force of the IEF under irradiation (Fig. 3a). The photo-deposition of Pt nanoparticles was also performed to confirm the charge transfer direction under light irradiation, as Pt^{4+} in H_2PtCl_6 can be reduced to form Pt nanoparticles by photo-generated electrons. Therefore, Pt nanoparticles assemble in the electron-accumulation region[36]. Pt nanoparticles were clearly observed on the surface of $CuInS_2$ QDs (Supplementary Fig. 26), suggesting the transfer of photo-generated electrons from BiOCl and ultimately accumulated on $CuInS_2$ QDs, coinciding with the Z-scheme charge migration direction (Supplementary Fig. 27).

To gain deep insight into the charge separation and transfer behaviours, a series of stable-state and transient spectroscopy and electrochemical measurements were performed. UV–visible diffuse reflectance spectra demonstrated enhanced light absorption of $CuInS_2$/BiOCl compared with pristine BiOCl (Supplementary Fig. 28), suggesting the generation of more excitons. The highest photocurrent (Supplementary Fig. 29) and the smallest arc radius of the electrochemical impedance spectroscopy plots of $CuInS_2$/BiOCl (Supplementary Fig. 10) implied its improved charge separation and lower charge transfer resistance due to the Z-scheme heterojunction. Photoluminescence (PL) measurements further substantiated the above result. Under 325-nm excitation, BiOCl and $CuInS_2$/BiOCl showed PL emission in the range of 400–600 nm, attributed to the recombination of charge carriers in BiOCl (Fig. 3e). The $CuInS_2$/BiOCl composites exhibited pronounced PL quenching compared with BiOCl and $CuInS_2$ QDs (Fig. 3e and Supplementary Fig. 30), indicating the markedly enhanced charge transfer after the formation of the Z-scheme heterojunction[37]. Time-resolved PL (TRPL) measurements were conducted to further evaluate the charge transfer dynamics (Fig. 3f). $CuInS_2$/BiOCl showed a longer average PL lifetime (7.7 ± 0.2 ns) than that of BiOCl (3.2 ± 0.1 ns), suggesting that the formed Z-scheme heterojunction facilitated interfacial charge transfer separation, thus promoting photocatalytic processes[38].

To unravel the influence of the formed IEF on the charge transport dynamics, we measured the femtosecond transient absorption (fs-TA) spectra of BiOCl, $CuInS_2$ QDs and $CuInS_2$/BiOCl (Fig. 3g–l and Supplementary Fig. 31). By using a femtosecond UV–visible-light pump/white-light continuum probe scheme, we investigated the ultrafast charge transfer process between BiOCl and $CuInS_2$ QDs (Fig. 3g–i). The pump wavelength was first chosen at 320 nm, which ensured

https://doi.org/10.1038/s44221-026-00590-4

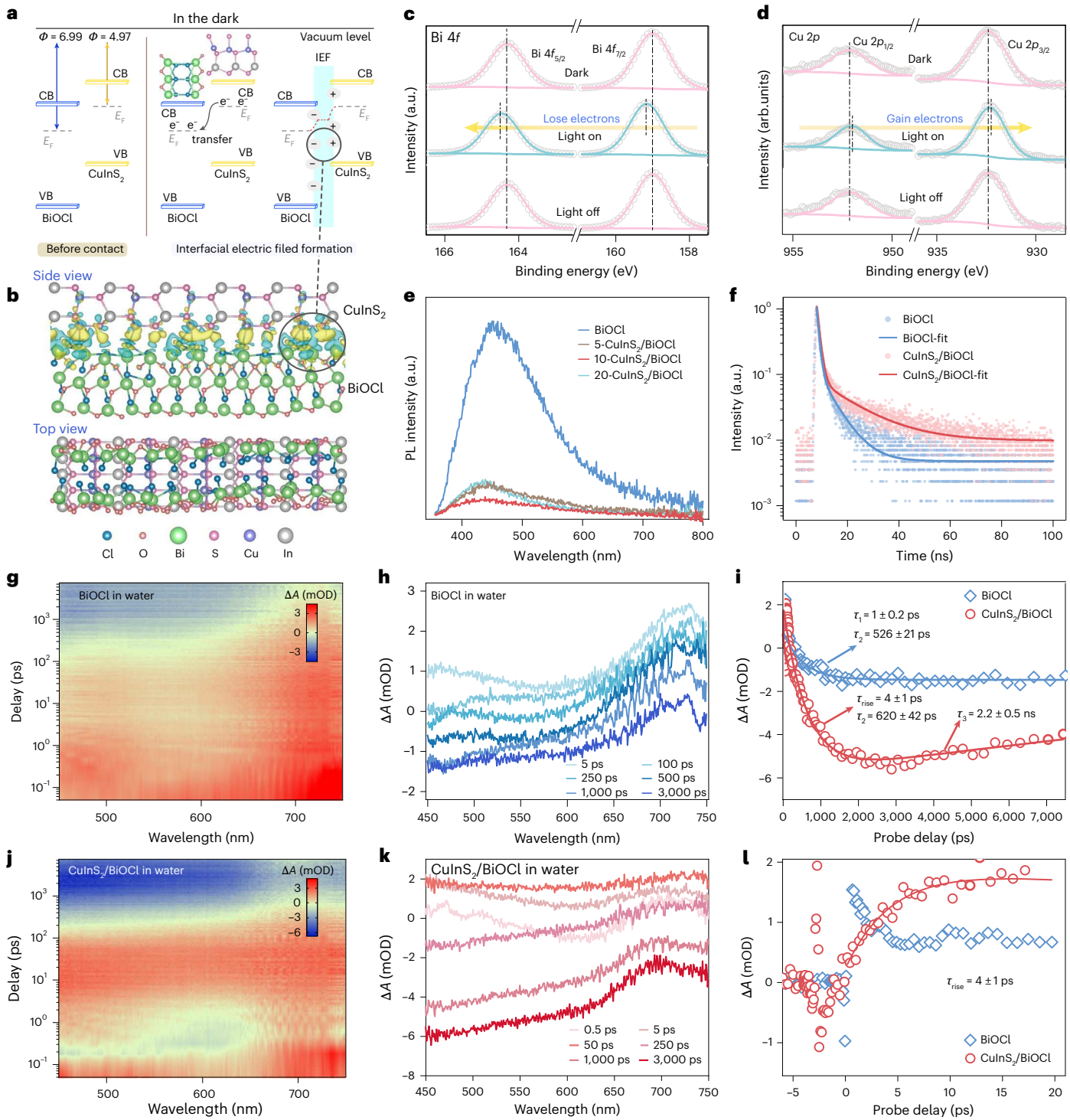

Fig. 3 | Charge-transfer direction and dynamics of Z-scheme heterojunction. **a**, A schematic illustration of the formation of IEF. **b**, Simulated charge distributions of the $CuInS_2$/BiOCl interface at Fermi level equilibrium. **c**,**d**, High-resolution Bi 4*f* (**c**) and Cu 2*p* (**d**) XPS spectra of $CuInS_2$/BiOCl before, during or after light illumination. **e**,**f**, PL (**e**) and TRPL spectra (**f**) of BiOCl and $CuInS_2$/BiOCl. **g**,**h**,**j**,**k**, Two-dimensional pseudo-colour TA spectra (**g**,**j**) and TA spectra (**h**,**k**) at different time slice of BiOCl (**g**,**h**) and $CuInS_2$/BiOCl (**j**,**k**). **i**,**l**, TA kinetics of BiOCl (blue squares) and $CuInS_2$/BiOCl (red circles) probed at ~550 nm. The blue and red solid lines are their fits.

effective electron excitation in BiOCl and $CuInS_2$. On the basis of previous investigations[39], photoinduced absorption (PA, $\Delta A > 0$) within the wavelength range of 450–750 nm was investigated to reveal the electron transfer process in BiOCl/$CuInS_2$. For pristine BiOCl (Fig. 3g–l), photoexcitation generates a broad PA signal centred at ~740 nm, while the TA kinetics exhibit a rapid positive-to negative crossover, characterized by a biexponential decay: $\tau_1 = 1 \pm 0.2$ ps and $\tau_2 = 526 \pm 21$ ps. Notably, such a decay does not return to the baseline but instead approaches a persistent negative asymptote, approximately −1 milli-Optical Density (mOD), indicating that full recovery to a null signal, expected upon complete charge recombination, occurs on an ultralong timecale[40]. Such behaviour reflects a final recombination process with a lifetime

extending to the nanosecond-microsecond regime or longer. A biexponential decay in the picosecond domain is typically associated with the involvement of two trap states of different depths[41,42]. This behaviour is consistent with the photogenerated electron transfer from the CB to a shallow trap state (TS1) and subsequently to a deep trap state (TS2). The recombination of localized electrons in TS2 with holes is a long process lasting from nanosecond to microsecond or even longer[41].

As for $CuInS_2$/BiOCl, the transient absorption (TA) spectra (Fig. 3i–l) evolution differs markedly from that of pristine BiOCl. Whereas BiOCl exhibits a clear positive PA feature, the hybrid is dominated by a negative photo-bleaching signal (PB, $\Delta A < 0$) signal, primarily contributed by $CuInS_2$ (ref. 43), suggesting that excited-state electron dynamics are governed by the $CuInS_2$ domain. Remarkably, despite the much larger fraction of BiOCl than $CuInS_2$ and simultaneous excitation of both components at 320 nm, the characteristic BiOCl PA signal at ~740 nm nearly disappears in the hybrid. This result demonstrates that the photogenerated electrons in BiOCl do not accumulate but are rapidly transferred (Fig. 3k). Both BiOCl (521 ± 21 ps) and the $CuInS_2$/BiOCl (620 ± 42 ps) display decay component on the order of hundreds of picoseconds (Fig. 3i–l), assigned to electron trapping from TS1 to TS2 in BiOCl. Notably, a distinct decay component of 2.2 ± 0.5 ns appears exclusively in $CuInS_2$/BiOCl, which can be attributed to electron transfer from the TS2 in BiOCl to $CuInS_2$ as this decay process happens after electron trapping in TS2. By contrast, pristine BiOCl evolves towards a long-lived negative asymptote.

Early-time dynamics within the first 20 ps further differentiate the two systems. The TA signal of pristine BiOCl builds up within the instrument response function of 100 fs and decays in 1 ± 0.2 ps. In $CuInS_2$/BiOCl, the 1 ps decay process is replaced by a pronounced signal growth with a longer timescale (4 ± 1 ps) than the instrument response function (Fig. 3l). Such a delayed buildup before relaxation is known as a spectroscopic fingerprint of band-edge electron transfer across heterojunctions[44,45], here demonstrating a Z-scheme transfer from the CB of BiOCl to $CuInS_2$. Importantly, this process occurs before trapping in BiOCl as the electrons in CB are delocalized. CB electrons (4 ± 1 ps) therefore migrate much faster than those released from TS2 (2.2 ± 0.5 ns).

Overall, these results demonstrate two sequential electron transfer channels in the $CuInS_2$/BiOCl system, from the delocalized CB and the localized trap state of BiOCl to $CuInS_2$ (Supplementary Fig. 32). These processes collectively facilitate efficient charge separation and suppress e^-–h^+ recombination, thereby prolonging the charge carrier lifetime in the heterostructure[46], consistent with TRPL results (Fig. 3f).

Combining the stable-state and time-resolved measurements and DFT calculations, the formation of Z-scheme $CuInS_2$/BiOCl heterojunction was unambiguously verified (Supplementary Fig. 27). It allows oriented and rapid charge transfer and retains the strong redox capability of photo-generated reductive electrons in $CuInS_2$ and oxidative holes in BiOCl, demonstrating great potential for the photocatalytic decomposition of PFAS.

Mechanism of OBS degradation in water

To unveil the mechanism of the photocatalytic OBS degradation, reactive species generated in the $CuInS_2$/BiOCl system were analysed by electron paramagnetic resonance (EPR) spectroscopy and trapping experiments. EPR analysis was conducted with the addition of 5,5-dimethyl-1-pyrroline-*N*-oxide (DMPO) and 2,2,6,6-tetramethylpiperidine 1-oxyl (TEMPO) as trapping agents (Fig. 4a). DMPO-•OH signal was not detected, while the characteristic peaks of DMPO-$O_2^{\bullet-}$ were observed. The presence of e_{aq}^- was not observed in the EPR spectra, which excluded the contribution of e_{aq}^- to OBS defluorination (Supplementary Fig. 33).

As an EPR spin labelling with oxidative properties, TEMPO can be consumed by unpaired e^-. Its EPR signal attenuation is thus an indicator of the presence of photo-generated electrons[47,48]. Compared with dark conditions, the characteristic triplet peaks of TEMPO disappeared in the EPR spectrum under light irradiation, suggesting the production of photoexcited e^- by $CuInS_2$/BiOCl.

To validate the contributions of active species to the OBS degradation, trapping experiments were carried out by using $K_2Cr_2O_7$, benzoquinone, isopropanol and triethanolamine as the scavengers of e^-, $O_2^{\bullet-}$, •OH and h^+, respectively[49–51]. The k values of OBS degradation and D_F achieved by $CuInS_2$/BiOCl were measured in the presence of different scavengers (Fig. 4b and Supplementary Fig. 34). No noticeable change was observed for the k value and D_F when isopropanol was added compared with the control experiment, indicating the negligible contribution of •OH, which was consistent with the EPR result. In the presence of triethanolamine, D_F remained unchanged while k value substantially decreased from 0.371 to 0.007 min^{-1}. It suggested that h^+ mainly contributed to direct OBS degradation rather than defluorination. The addition of benzoquinone led to slight decreases in both k value and D_F by 0.009 min^{-1} and 16.6%, respectively, suggesting that $O_2^{\bullet-}$ contributed to both defluorination and oxidation of OBS, as it can serve as both an oxidizing ($O_2^{\bullet-}/H_2O_2$, 0.89 V versus reversible hydrogen electrode) and reducing ($O_2/O_2^{\bullet-}$, −0.33 V versus reversible hydrogen electrode) agent[52]. N_2/O_2 bubbling experiments further confirmed the slight contribution of $O_2^{\bullet-}$ (Supplementary Fig. 35). As expected, the presence of $K_2Cr_2O_7$ substantially suppressed the degradation (reduced 0.003 min^{-1}) and defluorination (reduced to 5%) of OBS by $CuInS_2$/BiOCl. The results confirmed that e^- played the most predominant role in the photocatalytic degradation of OBS, especially for its defluorination. With the higher CB position of $CuInS_2$ and lower VB position of BiOCl, the photo-generated e^- and h^+ possessed strong reducing and oxidizing capabilities, respectively. Through our rationally designed and constructed Z-scheme $CuInS_2$/BiOCl heterojunctions, the strong redox ability of the charge carriers was retained and thus contributed to the efficient defluorination and carbon chain breakage of OBS.

The fs-TA test was conducted to further investigate the contribution of photo-generated electrons to the OBS degradation in $CuInS_2$/BiOCl system. The pump wavelength was adjusted to 420 nm, by which e^- in $CuInS_2$ can be selectively excited. In this case, bare BiOCl produced no fs-TA signal, simply because its bandgap is greater than 2.95 eV (420 nm). The fs-TA spectra of $CuInS_2$/BiOCl-water (Fig. 4c–g) showed a negative PB signal, which reflected the exciton bleach feature at ~750 nm. According to previous studies[20,53], the PB signal has been attributed to electron-induced state filling. The subsequent recovery was characterized by single-exponential $\tau = 47 \pm 2$ ps for $CuInS_2$/BiOCl, which was attributed to the charge recombination process in $CuInS_2$ QDs[43]. By contrast, the decay process after the addition of OBS solution was biexponential decay: $\tau_1 = 2.8 \pm 0.2$ ps and $\tau_2 = 65 \pm 19$ ps. Such a change should be attributed to the opening of an additional electron transfer channel from $CuInS_2$ to OBS[43]. Notably, the signal indicating $e^- \rightarrow e_{aq}^-$ transition was not observed in either the $CuInS_2$/BiOCl-water or $CuInS_2$/BiOCl-OBS system. This is consistent with the EPR result and provides additional evidence to rule out the involvement of e_{aq}^- in the photocatalytic process. We then estimated the ultrafast electron transfer process as 2.8 ps. The electron transfer rate associated with this channel was estimated as $k_{ET} = 1/\tau_{1(CuInS2/BiOCl\text{-}OBS)} - 1/\tau_{(CuInS2/BiOCl\text{-}water)} = 3.3 \times 10^{11}\ s^{-1}$. On the basis of interfacial electron transfer dynamics extracted from TA spectroscopy, it can be concluded that e^- generated in $CuInS_2$/BiOCl transfers to OBS molecules and contributes to defluorination[54]. The effective consumption of e^- by OBS also prohibited the recombination of charge carriers in excited $CuInS_2$/BiOCl, extending the lifetime of photoinduced charge carriers (65 ps for $CuInS_2$/BiOCl-OBS versus 47 ps for $CuInS_2$/BiOCl-water).

The distribution of the electrostatic potential on the OBS molecule surface was analysed by quantum chemical calculations. As shown in Fig. 4h, the sulfonic acid group and its adjacent benzene ring of OBS possess high electron density, making these sites more susceptible to electrophilic attack by photo-generated h^+. This interpretation is

https://doi.org/10.1038/s44221-026-00590-4

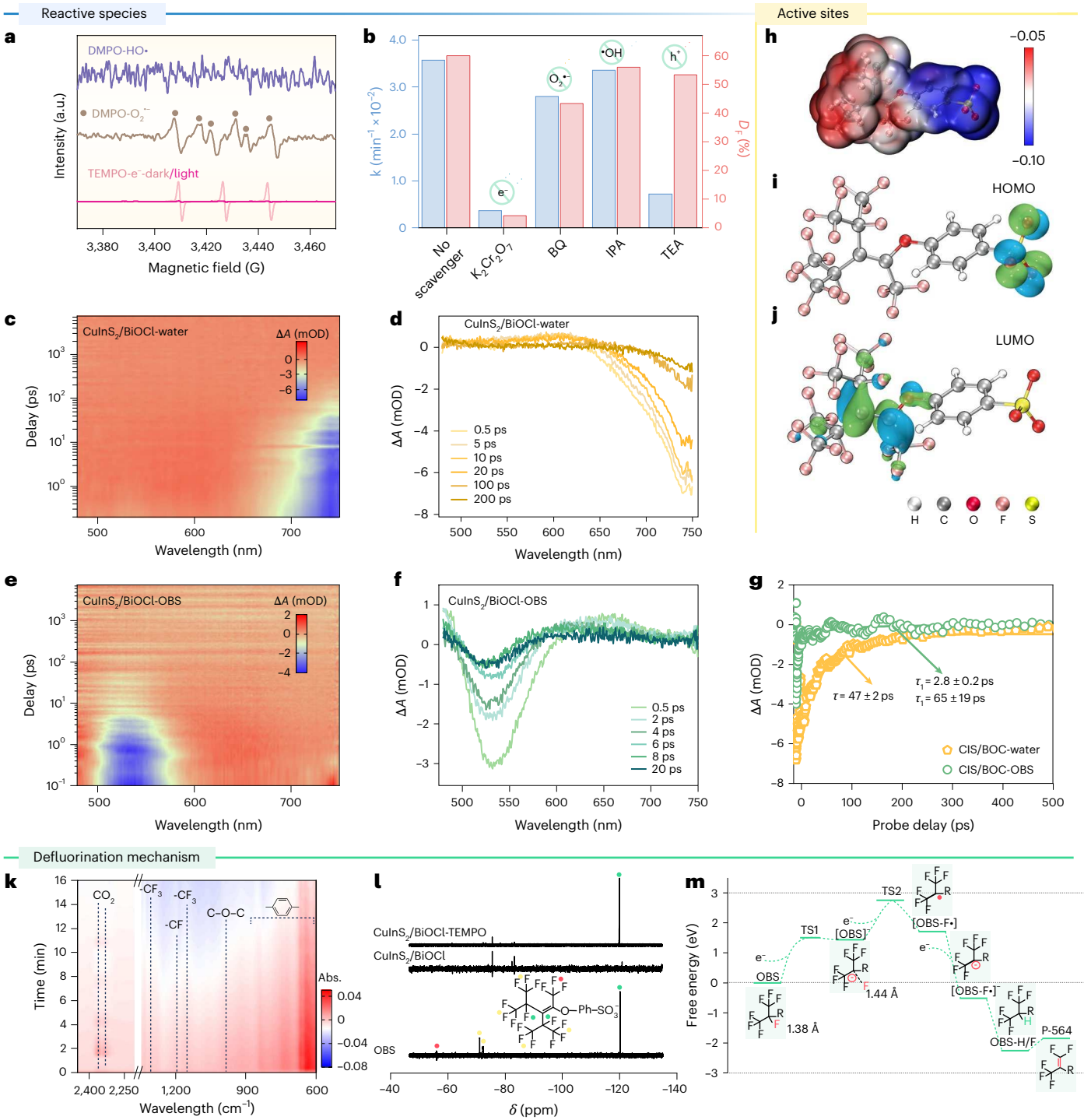

Fig. 4 | Identification of reactive species and the proposed mechanism of OBS degradation. a, EPR spectra in the presence of DMPO or TEMPO. **b**, OBS removal performance with the addition of different scavengers. **c**–**f**, Two-dimensional pseudocolor TA spectrum (**c**,**e**) and TA spectra (**d**,**f**) at different time slices of $CuInS_2$/BiOCl in water (**c** and **d**) and $CuInS_2$/BiOCl catalyst in OBS solution (**e** and **f**). **g**, TA kinetic of $CuInS_2$/BiOCl in water probed at ~730 nm (yellow circles) and $CuInS_2$/BiOCl catalyst in OBS solution probed at ~530 nm (green circles). The yellow and green solid lines are their fits. **h**–**j**, DFT calculations of OBS and the ESP distribution (**h**), LUMO orbitals (**i**) and HOMO orbitals (**j**) of OBS molecule. **k**, The two-dimensional intensity mapping of in situ FTIR spectra during photocatalytic degradation of OBS under simulated sunlight. Abs., represents absorption. **l**, ^{19}F NMR spectra of OBS after 24-h irradiation. **m**, Calculated free energy diagrams of H/F exchange reaction through OBS defluorination.

supported by >97% desulfonation efficiency within 5 h of simulated sunlight irradiation (Supplementary Fig. 36). The aromatic intermediates were detected (Supplementary Table 5 and Fig. 11), such as P-100, P-116, P-142, P-156 and P-164, suggesting the oxidative destruction of the aromatic ring by photogenerated holes. By contrast, the branched fluorinated carbon moiety exhibits relatively low electron density, and is more vulnerable to e^- attack[5]. The highest occupied molecular orbital (HOMO) and the lowest unoccupied molecular orbital (LUMO) are the active sites on organic molecules to interact with photo-generated holes and electrons, respectively[55]. The HOMO/LUMO locations (Fig. 4i,j) and orbital-weighted Fukui functions (Supplementary Table 8) of OBS were calculated to further reveal the

https://doi.org/10.1038/s44221-026-00590-4

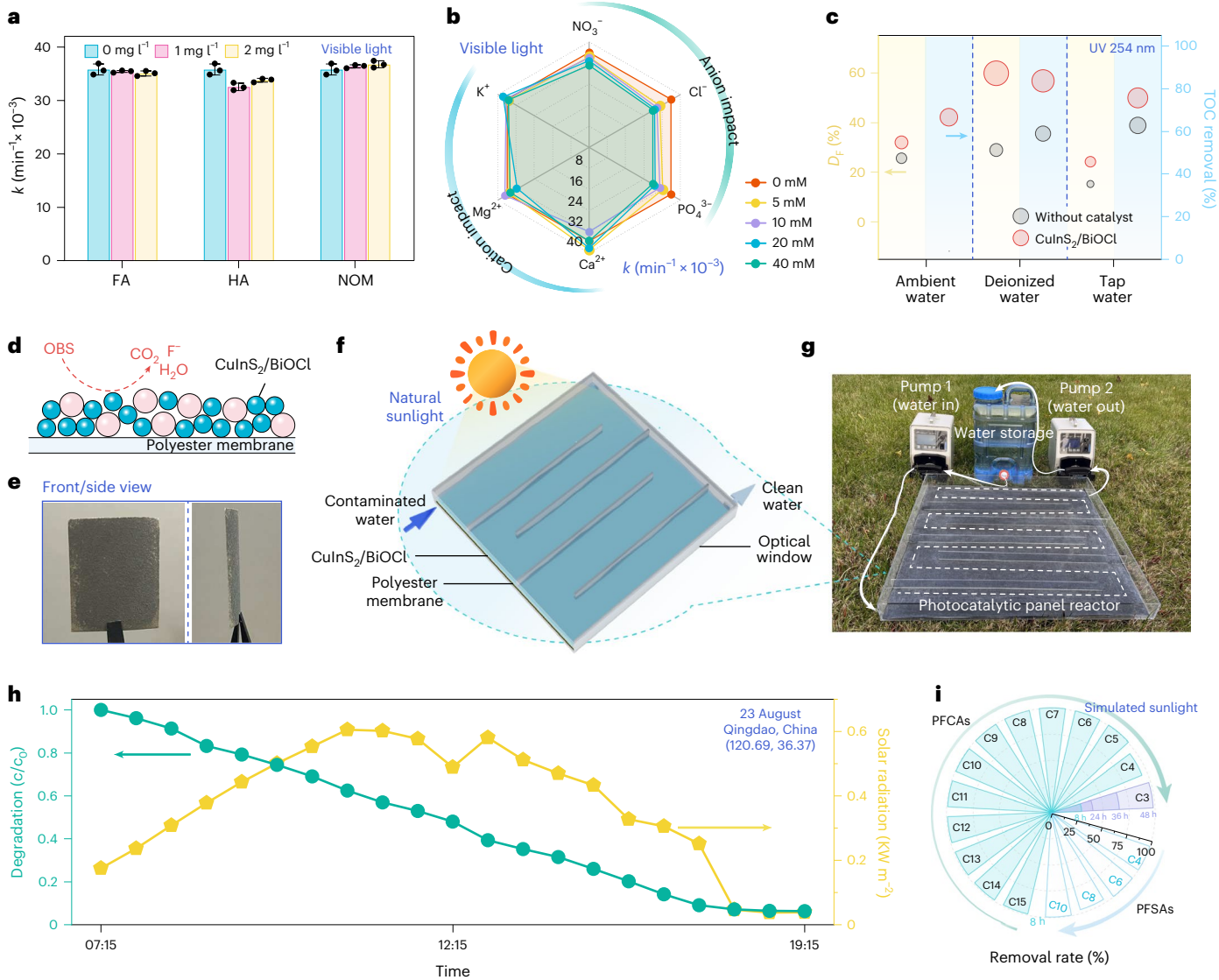

Fig. 5 | Utility and applicability of $CuInS_2$/BiOCl photocatalytic system. **a**,**b**, Effect of different DOM (**a**) and inorganic ions (**b**). **c**, Defluorination and mineralization of OBS by $CuInS_2$/BiOCl in various water metrics under 3-h UV (254 nm) irradiation. **d**, A schematic diagram of the solar-driven OBS removal by $CuInS_2$/BiOCl-coated polyester membrane. **e**, Photographs showing the front and side views of a $CuInS_2$/BiOCl-coated polyester membrane (2 × 2 cm^2). **f**, Illustration of the photocatalytic panel reactor. **g**, Photographic image of assembled photocatalytic system. **h**, Time courses of the OBS removal efficiency and solar illumination intensity during outdoor experiments in Qingdao, China. **i**, Degradation efficiency of PFAS mixture under simulated sunlight irradiation. The error bars in **a** were obtained by repeating the experiment three times and represent the standard deviations (mean values ± s.d., $n = 3$).

reactive sites for electrophilic and nucleophilic attack. The HOMO of OBS mainly consists of the sulfonic acid group, which showed a higher Fukui electrophilic index (f^-), indicating its high possibility for electrophilic attack by h^+ (ref. 56). C–F bonds constituted the LUMO of OBS and exhibited a higher Fukui nucleophilic index (f^+), suggesting that C–F bonds are prone to nucleophilic attack by e^- (ref. 56).

The structural evolution of OBS during photocatalysis was first examined by in situ Fourier-transform infrared spectroscopy (FTIR). As shown in Fig. 4k and Supplementary Fig. 38, the characteristic absorptions of $-CF_3$/–CF groups (1,266, 1,194 and 1,157 cm^{-1}), sulfonate (~1,027 and 1,349 cm^{-1})[57] and *para*-substituted aromatic ring (600–850 cm^{-1}) progressively decreased with irradiation. The peak at 982 cm^{-1} assigned to the ether bond disappeared within 8 min. These results suggested substantial destruction of the OBS molecular framework. HPLC coupled with high-resolution mass spectrometry (Supplementary Figs. 11 and 12 and Supplementary Table 5) analysis identified a series of intermediates and degradation products. Notably, the commonly acknowledged linear PFAS carbon chain shortening process (DHEH pathway) was not observed in the case of OBS[29]. The branched architecture of OBS renders multiple reactive sites susceptible to nucleophilic or electrophilic attack by reactive species during degradation. Among the identified intermediates, fragments indicating H/F exchange (for example, P-496 and P-564) were detected. This defluorination process was previously associated with e_{aq}^- in UV/sulfite systems[5]. Although e_{aq}^- was not detected in the photocatalytic system, it is hypothesized that photogenerated e^- may exert a similar effect, facilitating defluorination during OBS degradation. To further verify this hypothesis, time-dependent ^{19}F nuclear magnetic resonance (NMR) measurements were performed. As shown in Fig. 4l and Supplementary Fig. 39, the peaks corresponding to C(22)–F(28) and C(19)–F(35) disappeared within 8 h of irradiation, accompanied by the appearance of new fluorine resonances. By contrast, when photogenerated e^- were quenched by TEMPO, these C–F-associated signals remained detectable even after 24 h. These findings provide direct experimental evidence of

e^--mediated C–F bond breakage, which underlies the formation of intermediates such as P-583, P-496 and P-564. Theoretical simulations were performed to elucidate the H/F exchange pathway, emphasizing the e^--induced defluorination of OBS to produce P-564 (Fig. 4m). The results revealed that upon capturing photogenerated e^-, OBS formed a carbanion intermediate $[OBS]^-$, which elongated the C–F bond at the α position from ~1.38 to ~1.44 Å, thereby rendering it more prone to cleavage and generating [OBS-F•] radicals. The radical subsequently underwent another e^--capture step to yield $[OBS\text{-}F\bullet]^-$, followed by H atom substitution and triggered a second defluorination step at the β-position, yielding the C=C containing product (P-564). The calculated free energy change of −1.85 eV confirmed the high thermodynamic feasibility of this pathway. Importantly, this simulated mechanism was entirely consistent with the intermediates (P-583 and P-564) experimentally identified by HPLC coupled with high-resolution mass spectrometry (Supplementary Table 5 and Supplementary Fig. 11) and with the e^--induced C–F bond cleavage evidenced by ^{19}F NMR measurements (Fig. 4l and Supplementary Fig. 39). Collectively, these results provide coherent experimental and theoretical support for the photogenerated e^--initiated C–F bond activation and breakage during OBS degradation. Based on the experimental results and the above analysis, we proposed the possible degradation pathways of OBS by $CuInS_2$/BiOCl (Supplementary Fig. 40).

Solar-driven catalytic destruction of PFAS in water and practical applications

Inorganic ions and dissolved organic matter (DOM), such as fulvic acid (FA) and humic acid (HA) are ubiquitous in natural water, which could affect the degradation of OBS[58]. We thus performed additional experiments to study their impacts. The $CuInS_2$/BiOCl photocatalytic system effectively resisted the interference of natural water background factors such as Suwannee River FA, HA and natural organic matter (NOM) (Fig. 5a). The addition of Ca^{2+}, Mg^{2+}, K^+, NO_3^-, Cl^- and PO_4^{3-} showed negligible impact on OBS degradation (Fig. 5b). Considering the complexity of ambient water environment, OBS degradation was conducted in the real-world water samples collected from Xiaoqing River, close to a large fluorine chemical plant in Shandong Province, China (37.07° N, 117.93° E; see Supplementary Table 9 for details). $CuInS_2$/BiOCl showed enhanced D_F and TOC removal rates of OBS in the ambient water matrix, which were 1.32 and 1.26 times higher than those in tap water, respectively (Fig. 5c). The improvement may be attributed to the DOM in real water, such as indole, skatole and tryptamine, which can facilitate C–F cleavage of PFAS under UV exposure through enhancing the binding ability of reactive species source material with PFAS molecule[59]. To evaluate practical applicability, photocatalytic degradation of OBS with environmentally relevant levels was carried out (Supplementary Fig. 41). The negligible effect of initial concentrations on degradation performance demonstrated the robustness and practical potential of the $CuInS_2$/BiOCl system for PFAS removal from real-world water and wastewater.

Using powder photocatalysts for water treatment is challenged by the difficulty of separation and recycling. To overcome this issue, we fabricated centimetre-scale sheets loaded with $CuInS_2$/BiOCl powder (Fig. 5d,e) and devised a continuous-flow prototype reactor for the treatment of PFAS-contaminated water (Fig. 5f,g). A field test for OBS degradation was conducted under natural sunlight on the Qingdao Campus of Shandong University (from 7:15 to 17:15, 23 August 2024, Beijing time), achieving >96% OBS removal rate (Fig. 5h), with catalyst retention of 99.8%. The corresponding environmental parameters were summarized in Supplementary Fig. 42. To further simulate real application scenarios, the same outdoor setup was used to treat OBS-spiked real surface water sampled from a river near a fluorine chemical industry and semiconductor fabrication plant (37.07° N, 117.93° E, from 8:00 to 18:00, 10 September 2025, Beijing time). This system achieved a removal rate exceeding 76% after 10 h of natural sunlight irradiation (Supplementary Fig. 43), demonstrating its strong anti-interference properties and utility for treating PFAS-contaminated water in real-world scenarios. Given the prominent photo-redox efficiency of $CuInS_2$/BiOCl, we further studied the degradation of PFAS mixture (containing n = 3–15 PFCAs and n = 4, 6, 8, 10 PFSAs; see Supplementary Table 1 for details) under simulated sunlight (Fig. 5i). Over 94% removal of n = 4–15 PFCAs and PFSAs was achieved within 8 h (Fig. 5i and Supplementary Fig. 44). The removal efficiency of perfluorobutyric acid (n = 3) reached 29.0%, attributed to the high C–F bond dissociation energy[60,61]. Prolonged exposure to simulated sunlight resulted in a perfluorobutyric acid removal rate of >95%. To further evaluate applicability, we examined a mixture of short-chain PFCAs (C1–C7). All these PFCAs were completely degraded within ~16 h of simulated sunlight irradiation (Supplementary Fig. 45), demonstrating that the $CuInS_2$/BiOCl system is also effective for degrading short-chain PFAS, which are typically more recalcitrant. Zebrafish embryo toxicity tests demonstrated a substantial reduction in toxicity after the photocatalytic treatment (Supplementary Fig. 16). While the original PFCAs mixture completely inhibited hatching after 96 h, the treated solution allowed normal embryonic development with hatching rates comparable to those in pure water within 72 h. These results demonstrate the broad potential of the $CuInS_2$/BiOCl photocatalytic system for the removal of PFAS in real-world scenarios, particularly in the degradation of PFAS in surface waters.

Conclusion

We constructed a visible-light-responsive Z-scheme heterostructure by coupling BiOCl nanoplates with $CuInS_2$ QDs through inorganic S^{2-} ligands. This heterojunction achieves outstanding performance in the photocatalytic degradation of PFAS, with a defluorination efficiency of 75.8% and TOC removal of 76.8%, among the highest reported for PFAS degradation systems operating under UV light. The direct Z-scheme charge transfer pathway not only facilitates spatial charge separation via the established IEF, but also preserves strong redox potentials of photoinduced charge carriers for effective C–F and C–C bond cleavage. Experimental evidence, supported by DFT calculations, highlights the crucial role of photogenerated electrons in initiating the defluorination process. Experimental evidence, supported by DFT calculations, highlights the crucial role of photogenerated electrons in initiating the defluorination process. The $CuInS_2$/BiOCl exhibits robust adaptability and long-term stability across diverse water matrices and a mixture of 17 representative PFAS. Furthermore, its successful integration into a continuous-flow reactor operated under natural sunlight showcases a promising route towards practical, energy-efficient PFAS remediation. This work provides new physical insights into C–F bond activation under solar irradiation and enlightens the design of next-generation photocatalysts for PFAS decontamination in complex aqueous environments.

Methods

Synthesis of $CuInS_2$/BiOCl

The BiOCl and $CuInS_2$ QDs were prepared by the hydrothermal and hot-injection methods, respectively (see Supplementary Methods for details). A certain amount of $CuInS_2$ QDs (dissolved in *N*-methylformamide) was added to 20 mg of BiOCl and mixed by stirring for 10 min. A total of 20 ml of acetone was added to the mixture to enable the facilitated combination of $CuInS_2$ QDs with BiOCl. The precipitate was collected and washed with water. The purified precipitate was collected by centrifuge and dried at 60 °C for 8 h. By varying the added volumes of QD solution, $CuInS_2$/BiOCl with different loading mass fractions of $CuInS_2$ QDs were prepared, denoted as x-$CuInS_2$/BiOCl.

PFAS degradation experiments

The photocatalytic activity of the synthesized $CuInS_2$/BiOCl samples for OBS was carried out in a 100-ml quartz reactor connected to a

circulating water device that maintained the reaction temperature constant at 20 ± 0.2 °C. In a typical run, 25 mg sample was dispersed in 40-ml OBS solution (30 mg l^{-1}) followed by 90 min of dark stirring to reach adsorption–desorption equilibrium. Then, the solution was irradiated by a 300 W Xeon lamp (PerfectLight) equipped with an optical filter ($\lambda > 420$ nm). At predetermined time points, aliquots were extracted from the reaction solution and further filtered through 0.22-μm membrane. The pH value of the initial OBS solution (30 mg l^{-1}) was 6.36 ± 0.02.

The defluorination capacity and mineralization performance of the photocatalytic system were evaluated under simulated sunlight (300 W Xeon lamp, PerfectLight) or UV (20 W, Xingguang Electronic) irradiation. The reactor and temperature conditions used for the reaction were the same as described above. In this system, 100 mg of catalyst was mixed with 80 ml of OBS (30 mg l^{-1}). After stirring in the dark to reach adsorption equilibrium, it was irradiated under simulated sunlight or UV light for 24 h/8 h. The samples were aspirated at specific times and filtered through a 0.22-μm membrane for later analysis.

The degradation of a mixture of 17 representative PFAS was conducted using simulated sunlight (300 W Xeon lamp, PerfectLight) irradiation. Briefly, 40 ml of PFAS mixture (containing $n = 3–15$ PFCAs and $n = 4, 6, 8$ or 10 PFSAs, 1 mg l^{-1} for each reagent) was mixed with 25 mg of catalyst and was irradiated for 24 h after adsorption–desorption equilibrium.

Analysis methods

The concentration of OBS was qualified by HPLC (LC-20A, Shimadzu) equipped with a UV detector (275 nm). Separation was performed on a TC-C18 column (4.6 × 250 mm, 5 μm, Agilent) held at 45 °C and methanol/10 mM KH_2PO_4 (80/20, v/v) served as the mobile phase at 1.0 ml min^{-1}. The retention time of OBS is 7.7 min (Supplementary Fig. 46). The rate constant (k, min^{-1}) is obtained by a linear fitting of the $\ln(c_0/c)$ versus time function under first-order kinetics, where c_0 and c refer to the initial and reaction concentrations of OBS (mg l^{-1}).

Ion chromatography (ICS5000+, Thermo Fisher Scientific) was used for determining the concentrations of F^-. The retention time of F^- is 3.3 min (Supplementary Fig. 47). The defluorination rate (D_F) was calculated according to the following equation:

$$D_F(\%) = \frac{[F^-]}{[OBS]_{initial} \times n_{C-F}} \times 100\%. \quad (1)$$

$[F^-]$ signifies the reaction concentration of F^-. $[OBS]_{initial}$ represents the initial concentration of OBS, which is 30 mg l^{-1} in this study. n_{C-F} signifies the number of C–F bonds in OBS molecule, that is, 17.

The concentration of TOC was measured by a total organic analyser (TOC-L analyser, Shimadzu).

The reaction intermediates of OBS were analysed by HPLC combined with a high-resolution Q-TOF mass spectrometry (ImpactHD, Bruck). The mobile phase was ammonium acetate (2 mM) and methanol at a flow rate of 0.5 ml min^{-1}. The concentrations of representative PFAS were measured using an HPLC coupled with a 6470B triple quadrupole mass spectrometer (Agilent). The detailed methods for intermediates detection and PFAS quantification are shown in the Supplementary Methods.

Femtosecond pump–probe TA

The femtosecond pump–probe TA measurements were carried out on a regenerative amplified Ti: sapphire laser system (Coherent; 800 nm, 100 fs, 7 mJ per pulse and 1 kHz repetition rate) coupled to a HELIOS spectrometer (Ultrafast Systems LLC). A white-light continuum (450–750 nm) probe pulse was produced by focusing a small fraction of the 800-nm beam onto sapphire crystal. Pump–probe delays (0–8 ns) were controlled with a motorized optical delay stage. The pump beam was modulated at 500 Hz to record sequential pumped and unpumped spectra. BiOCl, $CuInS_2$/BiOCl and $CuInS_2$/BiOCl-OBS were dispersed in water, while $CuInS_2$ QDs sample was dispersed in toluene. All samples were placed in 2-mm quartz cuvettes and continuously stirred to maintain a fresh photoexcited volume during the course of the fs-TA measurements.

Computational details

DFT calculations for the solid-state systems were performed using the Vienna Ab Initio Package[62,63] within the generalized gradient approximation using the Perdew–Burke–Ernzerhof [64] formulation and projected augmented wave potentials[65,66]. A plane-wave cutoff of 400 eV was applied. Electronic occupancies were treated with Gaussian smearing (0.05 eV). The electronic self-consistency was achieved when total energy changes were lower than 10^{-5} eV and structural relaxations were converged when residual forces were less than 0.02 eV $Å^{-1}$. Long-range dispersion was included through the Grimme's DFT-D3 methodology[67].

Computations for OBS and related intermediates were conducted using Gaussian 16. The initial molecular structure of OBS was pre-optimized using the xtb package. Geometry and energy calculation employed the B3lyp[68,69] functional with 6-311+G(d,p) level with the SMD water solvation model. Refined structures and energies were then obtained by B3LYP/6-31g(d,p). The Fukui function analysis was based on Multiwfn changes and processed with Multiwfn.

Continuous-flow treatment of PFAS-containing water

To fabricate the photocatalytic sheet, $CuInS_2$/BiOCl was dispersed in isopropanol/0.5 wt% Nafion mixture (v/v: 9:1). SiO_2 particles were added to efficiently separate $CuInS_2$/BiOCl particles to build small interlayer gaps as reaction active sites[70]. The suspension was sonicated for 10 min to form a stable sol. The sol was drop-casted onto a one-side hydrophobic polyester membrane. The sheets were dried at 60 °C for 6 h.

The panel reactor was assembled using a commercial polypropylene plastic box (200 mm × 200mm × 40 mm). Polymethyl methacrylate partitions (180 mm × 10 mm × 30 mm) served the function of controlling the direction of water flow. $CuInS_2$/BiOCl-coated PTFE membranes were fixed on the bottom of a plastic box (Fig. 5e). Two peristaltic pumps and a water storage bottle (2 litres, 30 mg l^{-1} OBS solution) were used to simulate flowing PFAS-contaminated water at 40 ml min^{-1} (Fig. 5f). An outdoor photovoltaic solar panel was used to provide electricity for pumps, enabling fully solar-powered operation of the treatment system. Outdoor photocatalytic degradation experiments were conducted under natural sunlight at the Qingdao Campus of Shandong University. The first experiment was performed using the OBS solution prepared in deionized water (from 7:15 to 17:15, 23 August 2024, Beijing time). The second test was carried out for real surface water spiked with OBS (from 8:00 to 18:00, 10 September 2025, Beijing time). The real surface water was sampled from Xiaoqing River close to a fluorine chemical industry and electronic park of Shandong Province, China (37.07° N, 117.93° E). The possible adsorption contribution from SiO_2 and the reactor components was assessed by monitoring OBS concentration changes under dark conditions (Supplementary Fig. 48). Catalyst retention was quantified by determining the mass of catalyst detached into the effluent, using the following equation: catalyst retention (%) = [1 − (mass of catalyst in effluent/initial catalyst mass)] × 100%.

Statistics

Average values were calculated on the basis of experiments performed in triplicate, except for the outdoor experiment. The errors correspond to the standard deviation of data points from individual samples.

Reporting summary

Further information on research design is available in the Nature Portfolio Reporting Summary linked to this Article.

Data availability

All relevant data that support the findings of this research are presented in the Article and its Supplementary Information. Source data are provided with this paper. All other data are available from the authors upon reasonable request.

References

1. Evich, M. G. et al. Per- and polyfluoroalkyl substances in the environment. *Science* **375**, eabg9065 (2022).
2. Trang, B. et al. Low-temperature mineralization of perfluorocarboxylic acids. *Science* **377**, 839–845 (2022).
3. Washington, J. W. et al. Nontargeted mass-spectral detection of chloroperfluoropolyether carboxylates in New Jersey soils. *Science* **368**, 1103–1107 (2020).
4. Xiao, F. et al. Cross-national challenges and strategies for PFAS regulatory compliance in water infrastructure. *Nat. Water* **1**, 1004–1015 (2023).
5. Liu, L. et al. Degradation of OBS (sodium *p*-perfluorous nonenoxybenzenesulfonatee) as a novel per- and polyfluoroalkyl substance by UV/persulfate and UV/sulfite: fluorinated intermediates and treatability in fluoroprotein foam. *Environ. Sci. Technol.* **56**, 6201–6211 (2022).
6. Jin, B. et al. Substantial defluorination of polychlorofluorocarboxylic acids triggered by anaerobic microbial hydrolytic dechlorination. *Nat. Water* **1**, 451–461 (2023).
7. Zhang, B. et al. PFOS and its substitute OBS cause endothelial dysfunction to promote atherogenesis in ApoE$^{-/-}$ mice. *Environ. Health* **3**, 526–538 (2025).
8. Tu, W. Q. et al. Bioconcentration and metabolic effects of emerging PFOS alternatives in developing zebrafish. *Environ. Sci. Technol.* **53**, 13427–13439 (2019).
9. Yang, W. et al. Multiomic landscape of primary hypothyroidism induced by subchronic exposure to low-dose novel PFOS substitute OBS in human and murine models. *Environ. Sci. Technol.* **59**, 8329–8344 (2025).
10. Guan, Y. et al. Near-complete destruction of PFAS in aqueous film-forming foam by integrated photo-electrochemical processes. *Nat. Water* **2**, 443–452 (2024).
11. Gao, J. et al. Photochemical degradation pathways and near-complete defluorination of chlorinated polyfluoroalkyl substances. *Nat. Water* **1**, 381–390 (2023).
12. Zhang, H. et al. Photocatalytic low-temperature defluorination of PFASs. *Nature* **635**, 610–617 (2024).
13. Wen, Y. et al. Integrated photocatalytic reduction and oxidation of perfluorooctanoic acid by metal-organic frameworks: key insights into the degradation mechanisms. *J. Am. Chem. Soc.* **144**, 11840–11850 (2022).
14. Zhu, Y. et al. Photocatalytic degradation of GenX in water using a new adsorptive photocatalyst. *Water Res.* **220**, 118650 (2022).
15. Liu, Z. et al. Accelerated degradation of perfluorosulfonates and perfluorocarboxylates by UV/sulfite + iodide: reaction mechanisms and system efficiencies. *Environ. Sci. Technol.* **56**, 3699–3709 (2022).
16. Cui, J. et al. Destruction of per- and polyfluoroalkyl substances (PFAS) with advanced reduction processes (ARPs): a critical review. *Environ. Sci. Technol.* **54**, 3752–3766 (2020).
17. Zhao, D. et al. Boron-doped nitrogen-deficient carbon nitride-based Z-scheme heterostructures for photocatalytic overall water splitting. *Nat. Energy* **6**, 388–397 (2021).
18. Song, S. et al. A selective Au-ZnO/TiO_2 hybrid photocatalyst for oxidative coupling of methane to ethane with dioxygen. *Nat. Catal.* **4**, 1032–1042 (2021).
19. Shi, Y. et al. Visible Light-driven conversion of carbon-sequestrated seawater into stoichiometric CO and HClO with nitrogen-doped BiOCl atomic layers. *Angew. Chem. Int. Ed.* **135**, e202302286 (2023).
20. Wu, K. et al. Quasi-type II $CuInS_2$/CdS core/shell quantum dots. *Chem. Sci.* **7**, 1238–1244 (2016).
21. Guan, M. et al. Vacancy associates promoting solar-driven photocatalytic activity of ultrathin bismuth oxychloride nanosheets. *J. Am. Chem. Soc.* **135**, 10411–10417 (2013).
22. Chen, B. et al. Synthesis and hybridization of $CuInS_2$ nanocrystals for emerging applications. *Chem. Soc. Rev.* **52**, 8374–8409 (2023).
23. Ning, J. et al. Synthesis and optical properties of cubic chalcopyrite/hexagonal wurtzite core/shell copper indium sulfide nanocrystals. *J. Am. Chem. Soc.* **141**, 20516–20524 (2019).
24. Wang, J. et al. Nature of novel 2D van der Waals heterostructures for superior potassium ion batteries. *Adv. Energy Mater.* **10**, 2000884 (2020).
25. Lee, S. et al. Transformation from $Cu_{2-x}S$ nanodisks to $Cu_{2-x}S$@ $CuInS_2$ heteronanodisks via cation exchange. *Chem. Mater.* **28**, 3337–3344 (2016).
26. Zhao, L. et al. Engineering Co single atoms in ultrathin BiOCl nanosheets for boosted CO_2 photoreduction. *Adv. Funct. Mater.* **35**, 2416346 (2025).
27. Liu, G. et al. Degradation of perfluorooctanoic acid with hydrated electron by a heterogeneous catalytic system. *Environ. Sci. Technol.* **56**, 6223–6231 (2021).
28. Liu, X. et al. Photochemical decomposition of perfluorochemicals in contaminated water. *Water Res.* **186**, 116311 (2020).
29. Glass, S. et al. Merits, limitations and innovation priorities for heterogeneous catalytic platforms to destroy PFAS. *Nat. Water* **3**, 644–654 (2025).
30. Yang, J. S. et al. New insight into PFOS transformation pathways and the associated competitive inhibition with other perfluoroalkyl acids via photoelectrochemical processes using GOTiO_2 film photoelectrodes. *Water Res.* **207**, 117805 (2021).
31. Gems, D. & Riddle, D. L. Longevity in *Caenorhabditis elegans* reduced by mating but not gamete production. *Nature* **379**, 723–725 (1996).
32. Gao, Z. et al. Defect-modulated oxygen adsorption and Z-scheme charge transfer for highly selective H_2O_2 photosynthesis in pure water. *Nat. Commun.* **16**, 8889 (2025).
33. Ben, H. et al. Diffusion-controlled Z-scheme-steered charge separation across PDI/BiOI heterointerface for ultraviolet, visible, and infrared light-driven photocatalysis. *Adv. Funct. Mater.* **31**, 2102315 (2021).
34. Meng, Z. et al. Kelvin probe force microscopy reveals spatially resolved charge-transfer mechanism in CdS/BiOBr S-scheme heterojunction photocatalyst. *Angew. Chem. Int. Ed.* **64**, e202505456 (2025).
35. Zhang, C. et al. Charge separation by creating band bending in metal–organic frameworks for improved photocatalytic hydrogen evolution. *Angew. Chem. Int. Ed.* **61**, e202204108 (2022).
36. Luo, Z. et al. Unveiling the charge transfer dynamics steered by built-in electric fields in BiOBr photocatalysts. *Nat. Commun.* **13**, 2230 (2022).
37. Ye, M. Y. et al. 0D/2D Heterojunctions of vanadate quantum dots/graphitic carbon nitride nanosheets for enhanced visible-light-driven photocatalysis. *Angew. Chem. Int. Ed.* **56**, 8407–8411 (2017).
38. Zhang, Q. et al. Ice-assisted synthesis of black phosphorus nanosheets as a metal-free photocatalyst: 2D/2D heterostructure for broadband H_2 evolution. *Adv. Funct. Mater.* **29**, 1902486 (2019).

39. Chen, Z. et al. Determining the charge-transfer direction in a p–n heterojunction BiOCl/g-C_3N_4 photocatalyst by ultrafast spectroscopy. *ChemPhotoChem* **1**, 350–354 (2017).
40. Yue, X. Z. et al. Directional electron-transfer channels via intramolecular donor–acceptor engineering in poly(heptazine imide) photoanodes for efficient water oxidation. *Appl. Catal. B* **383**, 126086 (2026).
41. Wheeler, D. A. & Zhang, J. Z. Exciton dynamics in semiconductor nanocrystals. *Adv. Mater.* **25**, 2878–2896 (2013).
42. Wang, H. et al. Oxygen-vacancy-mediated exciton dissociation in BiOBr for boosting charge-carrier-involved molecular oxygen activation. *J. Am. Chem. Soc.* **140**, 1760–1766 (2018).
43. Han, Y. et al. Triplet sensitization by 'self-trapped' excitons of nontoxic $CuInS_2$ nanocrystals for efficient photon upconversion. *J. Am. Chem. Soc.* **141**, 13033–13037 (2019).
44. Lei, F. et al. Atomic-layer-confined doping for atomic-level insights into visible-light water splitting. *Angew. Chem. Int. Ed.* **127**, 9398–9402 (2015).
45. Li, R. et al. Integration of an inorganic semiconductor with a metal–organic framework: a platform for enhanced gaseous photocatalytic reactions. *Adv. Mater.* **26**, 4783–4788 (2014).
46. Chen, X. et al. Efficient photocatalytic overall water splitting induced by the giant internal electric field of a g-C_3N_4/rGO/PDIP Z-scheme heterojunction. *Adv. Mater.* **33**, 2007479 (2021).
47. Dong, X. A. et al. Insights into dynamic surface bromide sites in $Bi_4O_5Br_2$ for sustainable N_2 photofixation. *Angew. Chem. Int. Ed.* **61**, e202200937 (2022).
48. Ma, J. et al. Functional B@*m*CN-assisted photocatalytic oxidation of biomass-derived pentoses and hexoses to lactic acid. *Green Chem.* **22**, 6384–6392 (2020).
49. Huo, Z. Y. et al. Triboelectrification induced self-powered microbial disinfection using nanowire-enhanced localized electric field. *Nat. Commun.* **12**, 3693 (2021).
50. Gebre, S. T. et al. Amine hole scavengers facilitate both electron and hole transfer in a nanocrystal/molecular hybrid photocatalyst. *J. Am. Chem. Soc.* **145**, 3238–3247 (2023).
51. Qiu, J. et al. COF/In_2S_3 S-scheme photocatalyst with enhanced light absorption and H_2O_2-production activity and fs-TA investigation. *Adv. Mater.* **36**, 2400288 (2024).
52. Lu, X. et al. Boosted charge transfer for highly efficient photosynthesis of H_2O_2 over Z-scheme I^-/K^+ co-doped g-C_3N_4/metal–organic-frameworks in pure water under visible light. *Adv. Energy Mater.* **14**, 2401873 (2024).
53. Lian, S. et al. Powering a CO_2 reduction catalyst with visible light through multiple sub-picosecond electron transfers from a quantum dot. *J. Am. Chem. Soc.* **139**, 8931–8938 (2017).
54. Tan, S. et al. Unravelling the structure-dependent defluorination mechanisms of per- and polyfluoroalkyl substances by hydrated electrons in UV/sulfite. *Nat. Water* **3**, 734–745 (2025).
55. Wang, A. et al. Enhanced and synergistic catalytic activation by photoexcitation driven S-scheme heterojunction hydrogel interface electric field. *Nat. Commun.* **14**, 6733 (2023).
56. Mao, Y. et al. Efficient reduction-oxidation coupling degradation of nitroaromatic compounds in continuous flow processes. *Nat. Commun.* **15**, 6364 (2024).
57. Sun, R. et al. New insights into thermal degradation products of long-chain per- and polyfluoroalkyl substances (PFAS) and their mineralization enhancement using additives. *Environ. Sci. Technol.* **58**, 22417–22430 (2024).
58. Zhou, Q. et al. Generating dual-active species by triple-atom sites through peroxymonosulfate activation for treating micropollutants in complex water. *Proc. Natl Acad. Sci.* **120**, e2300085120 (2023).
59. Chen, Z. et al. Highly efficient hydrated electron utilization and reductive destruction of perfluoroalkyl substances induced by intermolecular interaction. *Environ. Sci. Technol.* **55**, 3996–4006 (2021).
60. Xin, X. et al. Degradation and defluorination of per- and polyfluoroalkyl substances by direct photolysis at 222 nm. *ACS ES&T Water* **3**, 2776–2785 (2023).
61. Bentel, M. J. et al. Defluorination of per- and polyfluoroalkyl substances (PFASs) with hydrated electrons: structural dependence and implications to pfas remediation and management. *Environ. Sci. Technol.* **53**, 3718–3728 (2019).
62. Kresse, G. & Furthmüller, J. Efficiency of ab-initio total energy calculations for metals and semiconductors using a plane-wave basis set. *Comput. Mater. Sci.* **6**, 15–50 (1996).
63. Kresse, G. & Furthmüller, J. Efficient iterative schemes for ab initio total-energy calculations using a plane-wave basis set. *Phys. Rev. B* **54**, 11169 (1996).
64. Perdew, J. P. et al. Generalized gradient approximation made simple. *Phys. Rev. Lett.* **77**, 3865 (1996).
65. Kresse, G. & Joubert, D. From ultrasoft pseudopotentials to the projector augmented-wave method. *Phys. Rev. B* **59**, 1758 (1999).
66. Blöchl, P. E. Projector augmented-wave method. *Phys. Rev. B* **50**, 17953 (1994).
67. Grimme, S. et al. A consistent and accurate ab initio parametrization of density functional dispersion correction (DFT-D) for the 94 elements. *J. Chem. Phys.* **132**, 154104 (2010).
68. Becke, A. D. Density-functional thermochemistry. III. The role of exact exchange. *J. Chem. Phys.* **98**, 5648–5652 (1993).
69. Lee, C. et al. Accurate and simple analytic representation of the electron-gas correlation energy. *Phys. Rev. B* **37**, 785–789 (1988).
70. Teng, Z. et al. Atomically dispersed low-valent Au boosts photocatalytic hydroxyl radical production. *Nat. Chem.* **16**, 1250–1260 (2024).

Acknowledgements

We acknowledge the financial support from the National Natural Science Foundation of China (grant nos. 22376124 and 22206113 to Q.Z.), the Taishan Scholars Project Special Fund (grant no. tsqn202211039 to Q.Z.), the National Key Research and Development Program of China (grant no. 2024YFA0918804 to R.L.), Shandong Provincial Natural Science Foundation (grant no. ZR2023JQ007 to R.L.), Key R&D Program of Shandong Province, China (grant no. 2025CXPT017 to R.L.), Canada Research Chairs Program (grant no. CRC-2019-00253 to D.M.) and the Royal Society ISPF-International Collaboration Awards (grant no. ICA\R1\231046 to F.M.). We thank H. Sui, G. Lin and C. Zhang from the core facilities for life and environmental sciences, state key laboratory of microbial technology for the help and guidance in NMR, HPLC–tandem mass spectrometry and inductively coupled plasma mass spectrometry measurements. We appreciate the FTIR, HPLC–high-resolution mass spectrometry, TOC and ion chromatography measurements by M. Zhang, X. Su and X. Li from the Analytical Testing Center, School of Environmental Science and Engineering, Shandong University.

Author contributions

Q.Z. conceived and designed the study. Q.Z. and F.L. conducted the research and analysed the data. Q.S. and P.J.C. helped with the data fitting of EXAFS. Z.N., Y.H. and R.L. conducted the toxicity testing. Z.C. carried out the fs-TA measurements and analysed the resulting data. Q.Z., R.L., and X.D. supervised the entire research. Q.Z., F.L., H.L., Z.G., Y.Z., S.Y., C.G., F.M., Z.Z., Z.C., Y.Y., Y.C., D.M. and X.D. discussed the results. Q.Z. and F.L. wrote the manuscript. Q.Z., R.L., Z.C., Y.Y., Y.C., D.M. and X.D. revised the manuscript. All authors discussed and contributed to the manuscript.

Funding

Open access funding provided by Adelaide University.

Competing interests
The authors declare no competing interests. Readers are welcome to comment on the online version of the paper.

Additional information
Supplementary information The online version contains supplementary material available at https://doi.org/10.1038/s44221-026-00590-4.

Correspondence and requests for materials should be addressed to Runzeng Liu, Zongwei Chen, Xiaoguang Duan or Qingzhe Zhang.

Peer review information *Nature Water* thanks Zhurui Shen, Tianyuan Xu and the other, anonymous, reviewer(s) for their contribution to the peer review of this work.

[1]Shandong Key Laboratory of Environmental Processes and Health, Qingdao Key Laboratory of Marine Pollutant Prevention, School of Environmental Science and Engineering, Shandong University, Qingdao, China. [2]School of Chemical and Biomolecular Engineering and The University of Sydney Nano Institute, The University of Sydney, Sydney, New South Wales, Australia. [3]Shandong Provincial Key Laboratory of Animal Cell and Developmental Biology, School of Life Sciences, Shandong University, Qingdao, China. [4]Pritzker School of Molecular Engineering and the College, Department of Chemistry, The University of Chicago, Chicago, IL, USA. [5]Department of Chemistry and Centre for Processable Electronics, Imperial College London, White City Campus, London, UK. [6]State Key Laboratory of Pollution Control and Resource Reuse, School of Environment, Nanjing University, Nanjing, China. [7]Department of Chemical and Biological Engineering, Sir Robert Hadfield Building, The University of Sheffield, Sheffield, UK. [8]Institute of Frontier and Interdisciplinary Science, Shandong University, Qingdao, China. [9]Henan Institute of Advanced Technology, Zhengzhou University, Zhengzhou, China. [10]Centre Énergie Materiaux et Télécommunications, Institut National de la Recherche Scientifique, Varennes, Québec, Canada. [11]State Key Laboratory of Environmental Chemistry and Ecotoxicology, Research Center for Eco-Environmental Sciences, Chinese Academy of Sciences, Beijing, China. [12]Department of Chemistry and Biochemistry, Florida International University, Miami, FL, USA. [13]School of Chemical Engineering, The University of Adelaide, Adelaide, South Australia, Australia. ✉e-mail: rz.liu@sdu.edu.cn; zchen@zzu.edu.cn; xiaoguang.duan@adelaide.edu.au; qzz@sdu.edu.cn

nature portfolio

Corresponding author(s): Xiaoguang Duan

Last updated by author(s): 23/12/25

Reporting Summary

Nature Portfolio wishes to improve the reproducibility of the work that we publish. This form provides structure for consistency and transparency in reporting. For further information on Nature Portfolio policies, see our Editorial Policies and the Editorial Policy Checklist.

Statistics

For all statistical analyses, confirm that the following items are present in the figure legend, table legend, main text, or Methods section.

n/a	Confirmed
☐	☒ The exact sample size (*n*) for each experimental group/condition, given as a discrete number and unit of measurement
☐	☒ A statement on whether measurements were taken from distinct samples or whether the same sample was measured repeatedly
☒	☐ The statistical test(s) used AND whether they are one- or two-sided *Only common tests should be described solely by name; describe more complex techniques in the Methods section.*
☐	☒ A description of all covariates tested
☒	☐ A description of any assumptions or corrections, such as tests of normality and adjustment for multiple comparisons
☐	☒ A full description of the statistical parameters including central tendency (e.g. means) or other basic estimates (e.g. regression coefficient) AND variation (e.g. standard deviation) or associated estimates of uncertainty (e.g. confidence intervals)
☒	☐ For null hypothesis testing, the test statistic (e.g. *F*, *t*, *r*) with confidence intervals, effect sizes, degrees of freedom and *P* value noted *Give P values as exact values whenever suitable.*
☒	☐ For Bayesian analysis, information on the choice of priors and Markov chain Monte Carlo settings
☒	☐ For hierarchical and complex designs, identification of the appropriate level for tests and full reporting of outcomes
☒	☐ Estimates of effect sizes (e.g. Cohen's *d*, Pearson's *r*), indicating how they were calculated

Our web collection on statistics for biologists contains articles on many of the points above.

Software and code

Policy information about availability of computer code

Data collection	Chromeleone 7.2; Bruker DataAnalysis 4.2; CHI660E; Agilent MassHunter10.0
Data analysis	OriginPro 2023b; Gatan DigitalMicrograph 3.1; Bruker DataAnalysis 4.2; Graphpad prism 10.1.2; nanomeasure 1.2; Avantange 6.9; Chromeleone 7.2; masshunter 10.0

For manuscripts utilizing custom algorithms or software that are central to the research but not yet described in published literature, software must be made available to editors and reviewers. We strongly encourage code deposition in a community repository (e.g. GitHub). See the Nature Portfolio guidelines for submitting code & software for further information.

Data

Policy information about availability of data

All manuscripts must include a data availability statement. This statement should provide the following information, where applicable:

- Accession codes, unique identifiers, or web links for publicly available datasets
- A description of any restrictions on data availability
- For clinical datasets or third party data, please ensure that the statement adheres to our policy

All relevant data that support the findings of this research are presented in the main text and Supplementary information. Source data are provided with this paper. All other data are available from the authors upon reasonable request.

Research involving human participants, their data, or biological material

Policy information about studies with human participants or human data. See also policy information about sex, gender (identity/presentation), and sexual orientation and race, ethnicity and racism.

Reporting on sex and gender	N/A
Reporting on race, ethnicity, or other socially relevant groupings	N/A
Population characteristics	N/A
Recruitment	N/A
Ethics oversight	N/A

Note that full information on the approval of the study protocol must also be provided in the manuscript.

Field-specific reporting

Please select the one below that is the best fit for your research. If you are not sure, read the appropriate sections before making your selection.

☐ Life sciences ☐ Behavioural & social sciences ☒ Ecological, evolutionary & environmental sciences

For a reference copy of the document with all sections, see nature.com/documents/nr-reporting-summary-flat.pdf

Ecological, evolutionary & environmental sciences study design

All studies must disclose on these points even when the disclosure is negative.

Study description	The experiment involved the synthesis of high performance CuInS2/BiOCl Z-scheme heterostructure, the characterization of its basic properties and the removal of Per- and polyfluoroalkyl substances (PFAS). Triplicate reporting is done to ensure accuracy and precision in the results, as well as to validate the reproducibility of the experiment. By averaging the three measurements, random errors can be reduced and the overall reliability of the data can be improved. Additionally, it can help detect systematic errors in the experimental setup, data recording, or analysis.
Research sample	All research samples were synthesized and fabricated by the authors of the manuscript in the laboratory. The test samples of PFAS-polluted water with known concentration were prepared in the laboratory. Various control experiments were conducted to test the validity of our hypothesis or to determine the specific cause of an observed effect.
Sampling strategy	Samples were collected to track treated water chemistry with time.
Data collection	All experimental data were collected by the authors of the manuscript using specific apparatuses described in "Methods".
Timing and spatial scale	The indoor photocatalytic experiments was performed in the laboratory between Sep 1, 2022 - Apr 30, 2025. The outdoor experiment was conducted under natural sunlight in Qingdao, China on Aug 23, 2024 and Sep 10, 2025.
Data exclusions	No data were excluded form the analysis.
Reproducibility	Reported values are based on triplicates except for the outdoor experiment, where the values from the duplicates and a single experiment were reported, respectively. The errors correspond to the standard deviation of data points from individual samples. All attempts to repeat the experiment were successful.
Randomization	Randomization was not relevant in this study. Water treatment research typically involves complex design and testing that are difficult to randomly control and manipulate. Therefore, systematic and controlled experimentation were used over randomization in this study.
Blinding	Blinding was not applicable to this study as there was no experiments involving specific treatments or groups. Various control experiments were conducted to isolate and evaluate the impact of each variable.

Did the study involve field work? ☐ Yes ☒ No

Reporting for specific materials, systems and methods

We require information from authors about some types of materials, experimental systems and methods used in many studies. Here, indicate whether each material, system or method listed is relevant to your study. If you are not sure if a list item applies to your research, read the appropriate section before selecting a response.

Materials & experimental systems

n/a	Involved in the study
☒	☐ Antibodies
☒	☐ Eukaryotic cell lines
☒	☐ Palaeontology and archaeology
☐	☒ Animals and other organisms
☒	☐ Clinical data
☒	☐ Dual use research of concern
☒	☐ Plants

Methods

n/a	Involved in the study
☒	☐ ChIP-seq
☒	☐ Flow cytometry
☒	☐ MRI-based neuroimaging

Animals and other research organisms

Policy information about studies involving animals; ARRIVE guidelines recommended for reporting animal research, and Sex and Gender in Research

Laboratory animals	C. elegans (ethical applval was not required), zebra fish.
Wild animals	C. elegans N2 (Bristol): obtained from the Caenorhabditis Genetics Center (CGC). Zebrafish (Danio rerio): wild-type strain, bred and maintained in the laboratory facility.
Reporting on sex	C. elegans:hermaphrodite. Zebrafish: mixed adults used for breeding.
Field-collected samples	N/A
Ethics oversight	Experiments involving C. elegans and zebrafish embryos did not require ethical approval. C. elegans is not subject to institutional animal ethics oversight, and zebrafish embryos used in this study were all ≤120 hours post-fertilization, a developmental stage that is exempt from animal ethics review under standard institutional and international guidelines.

Note that full information on the approval of the study protocol must also be provided in the manuscript.

Plants

Seed stocks	N/A
Novel plant genotypes	N/A
Authentication	N/A